Journal of Power Sources 214 (2012) 21–27

Contents lists available at SciVerse ScienceDirect

Journal of Power Sources

journal homepage: www.elsevier.com/locate/jpowsour

Short communication

Facile synthesis of silicon films by photosintering as anode materials for lithium-ion batteries

Wei Chen [a], Nan Jiang [b,**], Zhongli Fan [a], Abirami Dhanabalan [a], Chunhui Chen [a], Yunjun Li [b], Mohshi Yang [b], Chunlei Wang [a,*]

[a] Department of Mechanical and Materials Engineering, Florida International University, Miami, FL 33174, USA
[b] Applied Nanotech Inc. (ANI), Austin, TX 78758, USA

ARTICLE INFO

Article history:
Received 16 March 2012
Received in revised form
5 April 2012
Accepted 7 April 2012
Available online 26 April 2012

Keywords:
Silicon film
Photosintering process
Lithium-ion batteries
Kapton foil

ABSTRACT

The silicon films as anode materials for lithium-ion batteries were fabricated by the cost-effective, high-throughput photosintering process. The thinner Si film (1.3 μm) exhibited larger storage capacity and better cyclability compared to the thicker one (4.2 μm) due to the close contact of the fused silicon nanoparticles with the substrate. Moreover, the addition of silver nanoparticles improved the conductivity of silicon film and facilitated the amorphous phase formation, resulting in enhanced capacity and cyclability. The photosintering approach highlights the advantage in the flexible and practicable manufacture and shows the promising prospects for developing high-performance Si-based anode materials.

1. Introduction

Lithium-ion batteries (LIB) with high energy density, high voltage and environmental friendliness have been widely used in the modern life [1,2]. Although such batteries are commercially successful, the rapid development of large electronic devices and (hybrid) electrical vehicles has defined a requirement for breaking through the capacity limits of commercialized graphite anode in LIB [3,4]. Some metals and semiconductors such as aluminum [5], tin [6], and silicon [7–9], which can react with lithium to form alloys and provide a specific capacity much higher than that of commercial graphite, have attracted great interest in recent years. Silicon is one of the attractive anode materials for LIB because it can provide a theoretical capacity as high as 4200 mAh g^{-1} ($Li_{4.4}Si$) [7]. However, large volume change of silicon upon insertion and extraction of lithium can cause pulverization and breakdown of the electrical conductive network, which results in rapid capacity fading [7,8]. In addition, the intrinsic poor conductivity of silicon may give rise to high cell resistance and low capacity [10]. Extensive efforts have been made to address such problems. It is reported that silicon thin film electrodes showed promising results related to specific capacity and cyclability [11–15]. Assembling ultrafine silicon anode materials into continuous film structures has been demonstrated to be an effective approach, which can not only reduce the dramatic volume changes, but also enhance contact area and suppress the movement of free particles. Various methods have been investigated such as chemical vapor deposition [11], vacuum evaporation [12], pulsed laser deposition [13], magnetron sputtering [14,15] to fabricate silicon thin film anode for LIB. For example, Takamura et al. reported that silicon film prepared by vacuum deposition showed a reversible capacity more than 2000 mAh g^{-1} over 1000 cycles [12]. Amorphous silicon thin film of 250 nm deposited using radio-frequency magnetron sputtering by Maranchi et al. exhibited an excellent reversible capacity of nearly 3500 mAh g^{-1} for 30 cycles [15]. However, developing a high throughput and cost-effective way to manufacture silicon film is still a great challenge. In current work, we present a facile, practical photosintering approach to obtain silicon films. In the photosintering process, a photosintering energy flash with optical power of 10^4 W cm^{-2} is used to cure silicon nanoparticles in a pulse ranging from hundreds of microseconds to 1 μs (Fig. 1). The fused silicon nanoparticles with controllable fusion degree can be realized by changing the amount of total energy delivered to the substrate, which improves the adhesion of as-prepared film with substrate. Moreover, photosintering approach also distinguishes

* Corresponding author. Tel.: +1 305 348 1217; fax: +1 305 348 1932.
** Corresponding author.
E-mail addresses: njiang@appliednanotech.net (N. Jiang), wangc@fiu.edu (C. Wang).

0378-7753/$ – see front matter © 2012 Elsevier B.V. All rights reserved.
doi:10.1016/j.jpowsour.2012.04.047

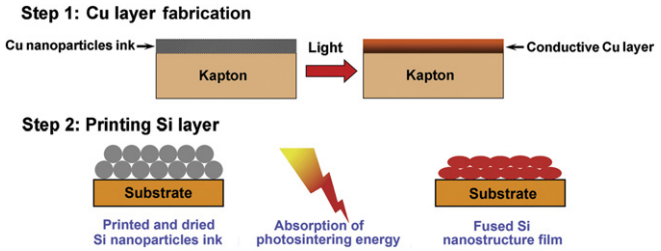

Fig. 1. The Schematic of photosintering process for Si films.

itself by the high throughput, both in manufacturing and in application. The photosintering exhibits high flexibilities in adjusting film thickness and adding auxiliary components, showing a promising application prospects.

2. Experimental section

2.1. Synthesis of silicon films by photosintering

Commercial polyimide film Kapton® was coated by ANI copper ink (Cu nanoparticles with particle size 20–100 nm formulated with the special dispersant and alcohol) and then dried in air at 100 °C for 10 min. The flashing light with the power density of 5.2 kW cm^{-2} was applied ~800 μs to obtain continuous Cu layer (See Electronic Supplementary Materials for the experimental details). Then silicon nanoparticles ink (Si nanoparticles with particle size 20–50 nm formulated with the special dispersant and alcohol) was coated on the above Cu-Kapton substrate, then dried and exposed with same operation conditions to form Si layer. The thickness was controlled by changing the viscosity of nano-Si ink and increasing the printing cycles. The ink with the viscosity of 400 cps and two printing cycles resulted in the Si layer with the thickness of ~4.2 μm, denoted as thick Si film in this work. The Si layer with the thickness of ~1.3 μm, denoted as thin Si film, was prepared with the 200 cps ink and one printing cycle. Furthermore, silver nanoparticle ink was added into above Si nanoparticle ink (for thin Si film) with the ink volume ratio of Ag/Si = 18/82 and treated by the same process to produce nano-Ag enhanced thin Si film with the same thickness of ~1.3 μm, affording the sample denoted as Si–Ag film.

2.2. Characterization of silicon films

Transmission electron microscopy image was obtained using a Tecnai T12 microscope (FEI Co.) operating at 120 kV. Field-emission scanning electron microscope (SEM) pictures were taken by a FEI Quanta 600 FEG, and the acceleration voltage was 30 kV. The film thickness was measured by AlphaStep 200 Surface Profiler, which has the vertical resolution of 15–20 nm. XRD was performed with Cu Ka radiation (λ = 1.54056 Å) on a Bruker D8 X-ray diffractometer. Raman spectroscopy measurements were carried out on a Horiba Aramis confocal microprobe Raman instrument with He–Cd laser (λ = 325 nm) and He–Ne laser (λ = 632.8 nm) at ~0.5 mW incident power.

2.3. Electrochemical measurements

The as-prepared thick Si, thin Si and Si–Ag films were cut into discs (Φ = 10 mm) and directly used as working electrodes, respectively. CR-2032-type coin cells were assembled in a glove box under argon atmosphere, where lithium discs were used as counter electrode and reference electrode. The electrolyte was 1 M lithiumbis(perfluoroethylsulfonyl)imide dissolved in the mixed solvent of ethylene carbonate: dimethyl carbonate: Diethyl carbonate in a 1:1:1 volume ratio. The electrochemical cells were galvanostatically cycled at room temperature by using an NEWARE BTS-610 battery tester. The current density of charge/discharge was 0.1 A g^{-1} in the voltage between 0.02 and 1.50 V (vs. Li/Li^+). The specific capacitance, as determined from galvanostatic charge/discharge curves, was calculated in accordance with the following equation:

$$C = I \times t/(\Delta V \times m)$$

where C is the specific capacitance of the samples, I is the current during discharge process, t is the discharge time, ΔV is the potential window, and m is the mass of the silicon films.

3. Results and discussion

Copper and silicon inks containing respective nanoparticles were prepared by Applied Nanotech Inc. (ANI) conductive ink technology. A non-destructive energy flash technique has been successfully used to cure metallic/nonmetallic nanoparticle inks to yield conductive films. As shown in the Schematic (step 1 in Fig. 1), the copper ink was firstly coated on commercially available Kapton® foils at room temperature, which were used as flexible substrate due to its mechanical stability, chemical inertness when exposed to the electrolyte and excellent adhesion with the photosintered Cu and Si nanoparticles. Then the Cu coating was exposed under special photosintering flash for a submicro-second to obtain conductive Cu layer in ANI's photosintering instrument, which uses high-intensity, short-pulse lamp to sinter nanoparticles on a very short period of time. In the printing Si layer process (step 2), Si nanoparticles ink was coated on the above Cu-Kapton substrate and exposed with photosintering flash to form Si layer. The whole fabricating process of Si film is rapid and easy to produce practical silicon anode materials cost-effectively.

Fig. 2(a) shows the typical photograph of as-prepared thick Si film with ~4.2 μm silicon layer and 0.315 mg cm^{-2} area density of silicon. Dark brown Si layer are uniformly printed on the substrate with the printing area as large as 100 by 65 mm. SEM image of cross section (Fig. 2(b)) shows that the Si layer is attached continuously on the copper/polyimide Kapton substrate. Moreover, the TEM image (Fig. 2(c)) of the powder scratched slightly from thick Si film demonstrates that most of Si nanoparticles are necking. The fused configuration is different from the crystalline feature of ball-like in Si ink, implying that the Si spheres can be sintered to be connected with each other under the high energetic flash.

Fig. 3 shows the SEM images of thick Si, thin Si and Si–Ag films. Thick Si film (~4.2 μm) exhibits porous structures (Fig. 3(a)). The Si nanoparticles are observed to be partly fused and the film surface is rough as shown in the inset. When the thickness of Si film is reduced to ~1.3 μm (Fig. 3(b)), due to the low viscosity of the ink, the silicon nanoparticles is dispersed evenly on the substrate and the as-produced film roughness is improved. The interspaces between the fused nanoparticles in thin film are similar to that in thick one, i.e., showing porous characteristic. As for thin Si–Ag film (Fig. 3(c)), the surface becomes flat and the porous interval is obviously reduced because the round and tiny (Ag) nanoparticles are embedded and dispersed among the relatively large fused Si particles.

XRD patterns of Kapton foil are displayed in Fig. 4(a). The intense peak at $2\theta = 21.5°$ and broad ones at 26.7° and 36.6° correspond to the characteristic diffraction peaks of Kapton. Declined baseline is observed in the range below 35° for Kapton foil. These features are preserved on the silicon films since the functional layers are based on the Kapton substrate (Fig. 4(b–d)). For the thick Si and thin Si

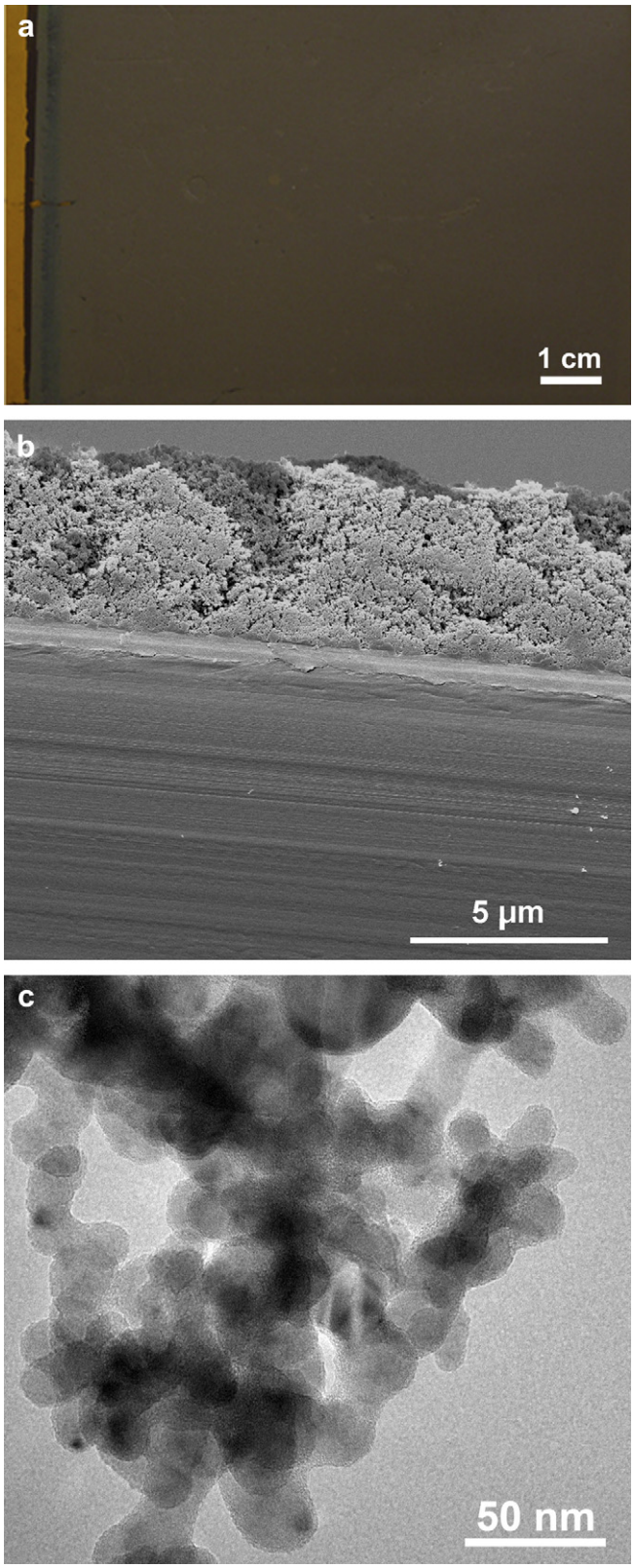

Fig. 2. (a) The typical photograph of the as-prepared thick Si film under optimized photosintering conditions: voltage: 1150 V; flashing power density: 6.2 kWcm^2. (b) The typical SEM image of cross section of the as-prepared thick Si film. (c) The TEM image of fused silicon particles obtained by scraping slightly from the surface of thick Si film.

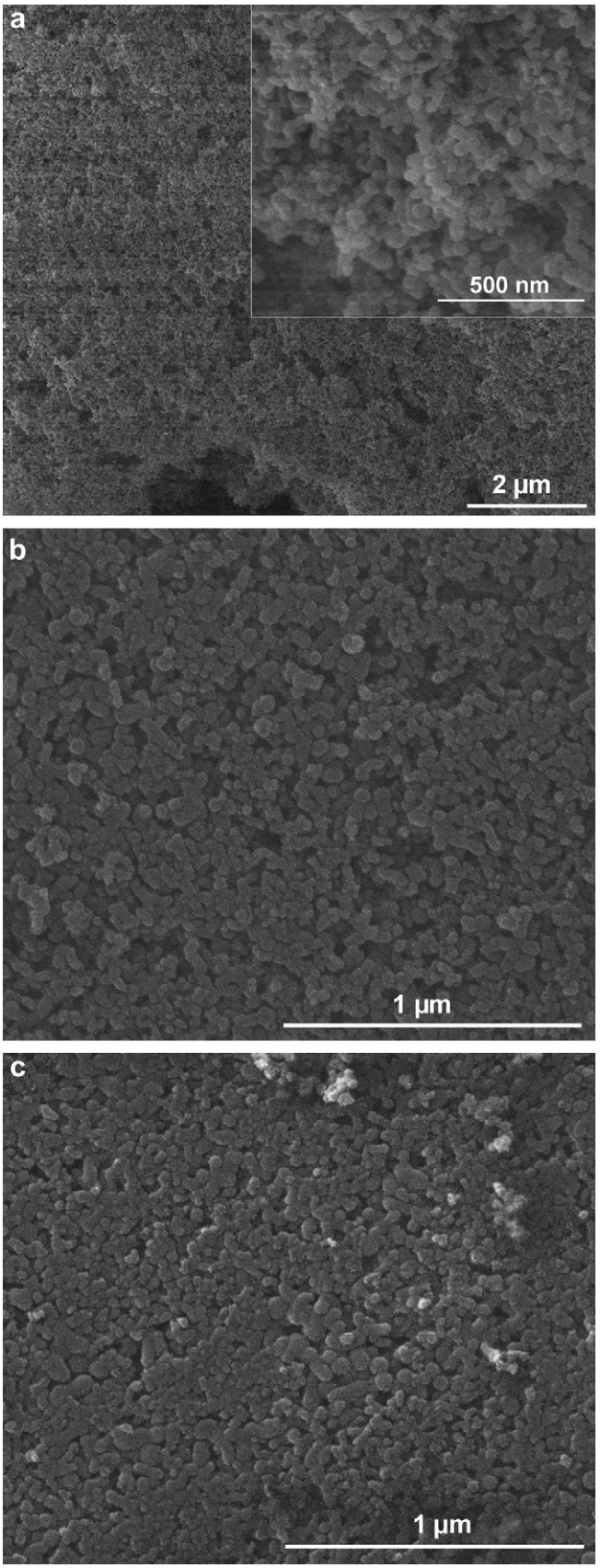

Fig. 3. SEM images of thick Si film (a), thin Si film (b) and Si–Ag film (c). The inset shows the corresponding high resolution images of individual films.

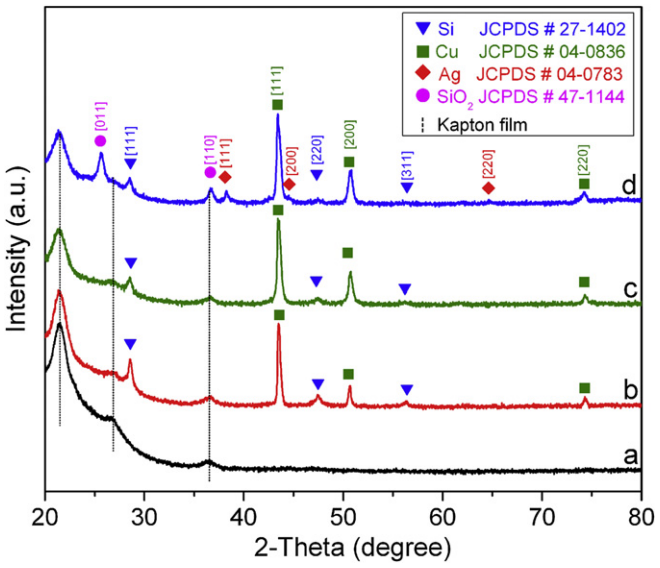

Fig. 4. XRD patterns of (a) Kapton foil, (b) thick Si film, (c) thin Si film and (d) Si–Ag film.

films (Fig. 4(b,c)), the diffraction peaks corresponding to Cu [111], [200] and [220] planes (JCPDS no. 04-0836, marked with squares) and Si [111], [220] and [311] planes (JCPDS no. 27-1402, marked with triangles) are detected. Moreover, it is notable that the relative intensity of Si/Cu in thin Si film is smaller than that in thick film, indicating the decreased ratio of Si in thin Si film. The peaks located in 38.2°, 44.5° and 64.7° (marked with diamonds) in Si–Ag film (Fig. 4(d)) can be assigned to Ag [111], [200] and [220] planes (JCPDS no. 04-0783), respectively. It is very interesting that two new peaks at 25.7° and 36.7° (marked with rounds) assigned to SiO_2 are detected in Si–Ag film. Considering the nature of catalytic oxidation of Ag, the presence of SiO_2 in Si–Ag film is reasonable because partial Si was catalytically oxidized to SiO_2 by Ag during the photosintering process.

Raman spectroscopy equipped by He–Cd and He–Ne lasers with excitation wavelength at 325 nm (Ultra-violet, UV) and 632.8 nm (visible) were used to study the composition of silicon films. For all samples, the Raman spectra show the asymmetry peak locates at ~510 cm^{-1}, which can be ascribed to LO–TO phonons of silicon [16]. It is reported that Raman spectra of silicon consists of two kinds of peaks, i.e., one at around 520 cm^{-1} originating from the crystalline silicon and another at around 480 cm^{-1} attributed to the amorphous phase [16–18]. The Raman bands of silicon films in the range of 390–560 cm^{-1} are fitted into two components, amorphous peak centered at 495 cm^{-1} and crystalline one at 520 cm^{-1}. The intensity (area) ratio of amorphous to crystalline phase (I_a/I_c) is use to distinguish the structure feature of Si films. The ratio of I_a/I_c for thick Si film is 0.72 and for thin Si film it is 0.73 under UV excitation (Fig. 5(a)), indicating almost same surface composition in silicon layer for thick and thin Si film. When Ag is added, the I_a/I_c ratio increases to 0.91, which implies more amorphous silicon phase in Si–Ag film compared to thin Si film. This demonstrates that the addition of silver affects the phase composition of silicon layer and facilitates the transformation of crystalline silicon to amorphous silicon, which is easily catalytically oxidized to form the silicon oxide, as evidenced by XRD results.

For visible Raman spectra, the I_a/I_c ratio of both thick and thin Si film is 0.39, while the value increases to 0.41 for Ag–Si film (Fig. 5(b)). Obviously, the I_a/I_c ratio under visible laser excitation is much lower than that under UV light excitation. As reported, the longer wavelength light is expected to penetrate deeper into the samples in the Raman characterization. The composition information of surface top region and bulk layer of silicon films, i.e., different depth of Si layer (<10 nm in Si at 325 nm versus 400 nm at visible laser), can be obtained using the different excitation wavelength of laser [19–21]. Using UV laser excitation, more signals come from the outmost silicon layer, while the bulk layer including surface can be detected by visible laser excitation. Lower I_a/I_c ratios under visible laser indicate that the bulk of silicon layer mainly comprises of crystalline Si phase and more amorphous structure exists in the surface of silicon films. In addition, the visible Raman spectra confirm that the addition of Ag increase the proportion of amorphous phase of silicon in the layer.

The galvanostatic discharge–charge curves and cyclability for thick Si film, thin Si film and Si–Ag film are shown in Fig. 6. These silicon films show a long slope plateau started from around 0.2 V in the discharge curve in the first cycle, which is the characteristic of Li_xSi alloy formation [22]. In the charge curves, the substrate polyimides cause the slope plateau formation starting at ~1.1 V from

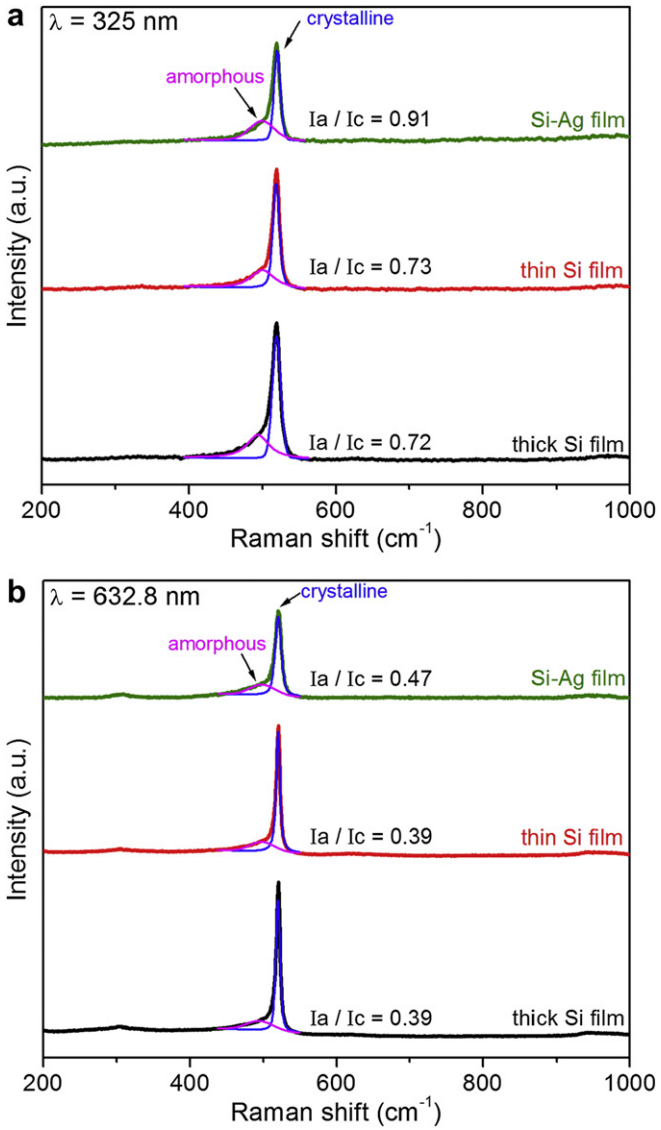

Fig. 5. The UV Raman spectra (a) and visible Raman spectra (b) of the thick Si film, thin Si film and Si–Ag film. The UV Raman spectra were obtained using 325 nm excitation wavelength, and visible Raman spectra using 632.8 nm excitation wavelength.

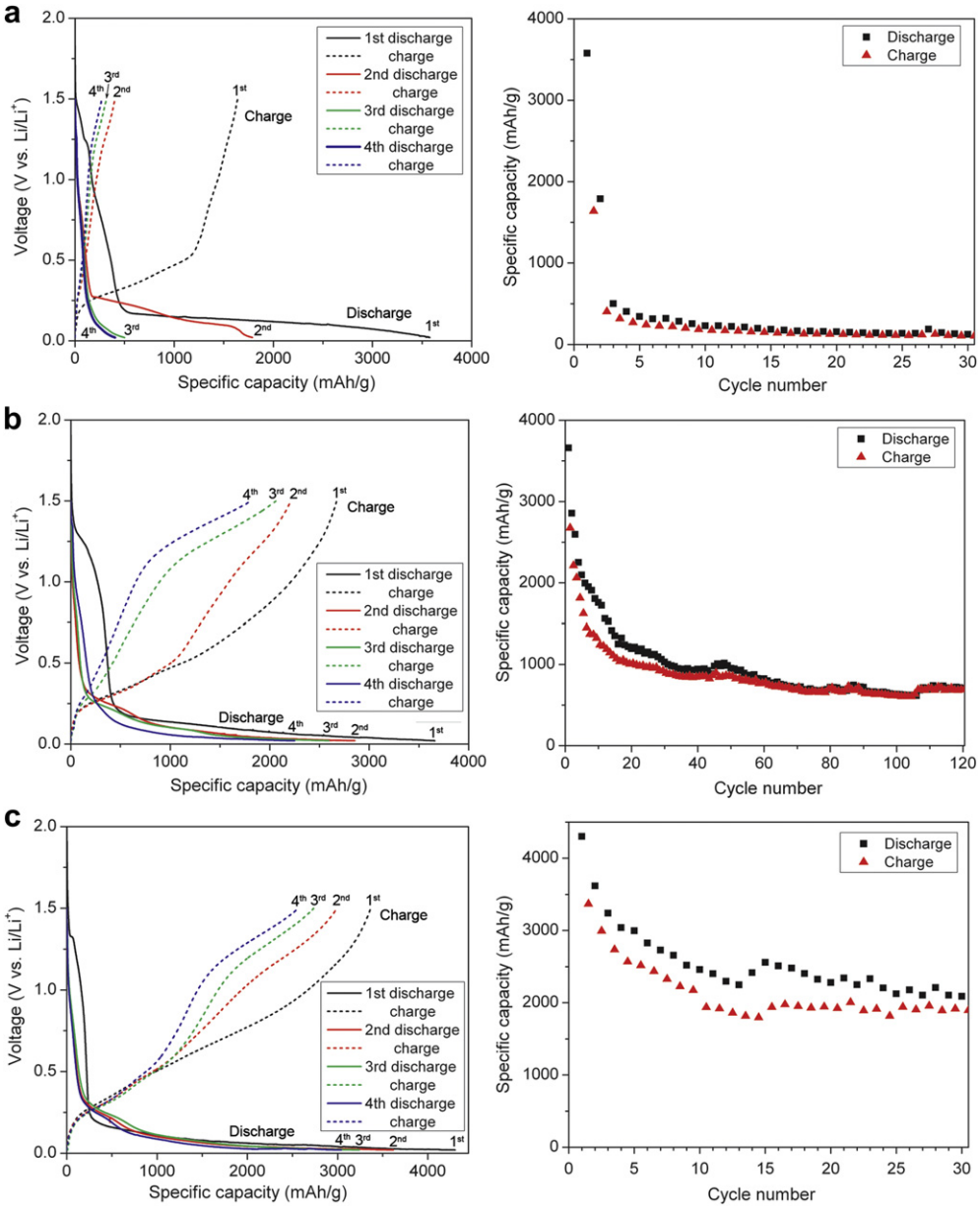

Fig. 6. Galvanostatic charge–discharge results of (a) thick Si film, (b) thin Si film and (c) Si–Ag film. The left part of each is the discharge–charge curves from the 1st to 4th cycle, while the right is the cycling performance of the films in the voltage range of 0.02–1.5 V.

the third cycle due to the lithiation of polyimide [23]. All the samples show the highest capacity at the first cycle. Then, the capacities drop rapidly in the second cycle due to the formation of solid electrolyte interface (SEI) layer. In the following cycles, the capacity fading rates become slow due to the stabilization of SEI layer. The initial specific discharge capacity of thick Si film is 3576 mAh g^{-1} and remains 125 mAh g^{-1} at the 30th cycle (the right part of Fig. 6(a)). When thickness of film is reduced to ~1.3 μm, the cyclability is improved greatly (Fig. 6(b)). The initial specific discharge of thin Si film is 3659 mAh g^{-1}, which is slightly higher than that of thick Si film. After 30 cycles, the specific discharge capacity of thin Si film maintains a reversible capacity of approximately 1029 mAh g^{-1}, which is almost eight times that of thick Si film at the 30th cycle. In the following cycles, the specific discharge capacity of thin Si film gradually decreases to 708 mAh g^{-1} at 120th cycle and about 31% loss of the specific capacity is observed relative to that of the 30th cycle. The improved cyclability of thin Si film might be attributed to its thinner film structure, which has better resistance to the stress caused by the lithium insertion/extraction, and hence the pulverization of the film is less severe than the thicker one. As plotted in Fig. 6(c), Si–Ag film displays the initial specific discharge capacity of 4301 mAh g^{-1}, which is much higher than that of thick Si film and thin Si film. XRD patterns show that there is silicon oxide in Si–Ag film, which might be responsible for the highest initial specific capacity due to the conversion reaction of oxide with lithium [24]. On the other hand, the surface oxide acting as buffer layer can suppress the volume expansion of silicon during the lithiation, which result in improved capacity retention [25,26]. After relatively slow fading, the capacity of Si–Ag film tends to stable and the reversible capacity is as high as 2090 mAh g^{-1} at the 30th cycle (Fig. 6(c)). It implies that the presence of Ag nanoparticles within thin silicon film can increase the electrical contact between fused silicon particles and benefit the electron transport of the film, resulting enhanced cyclability of

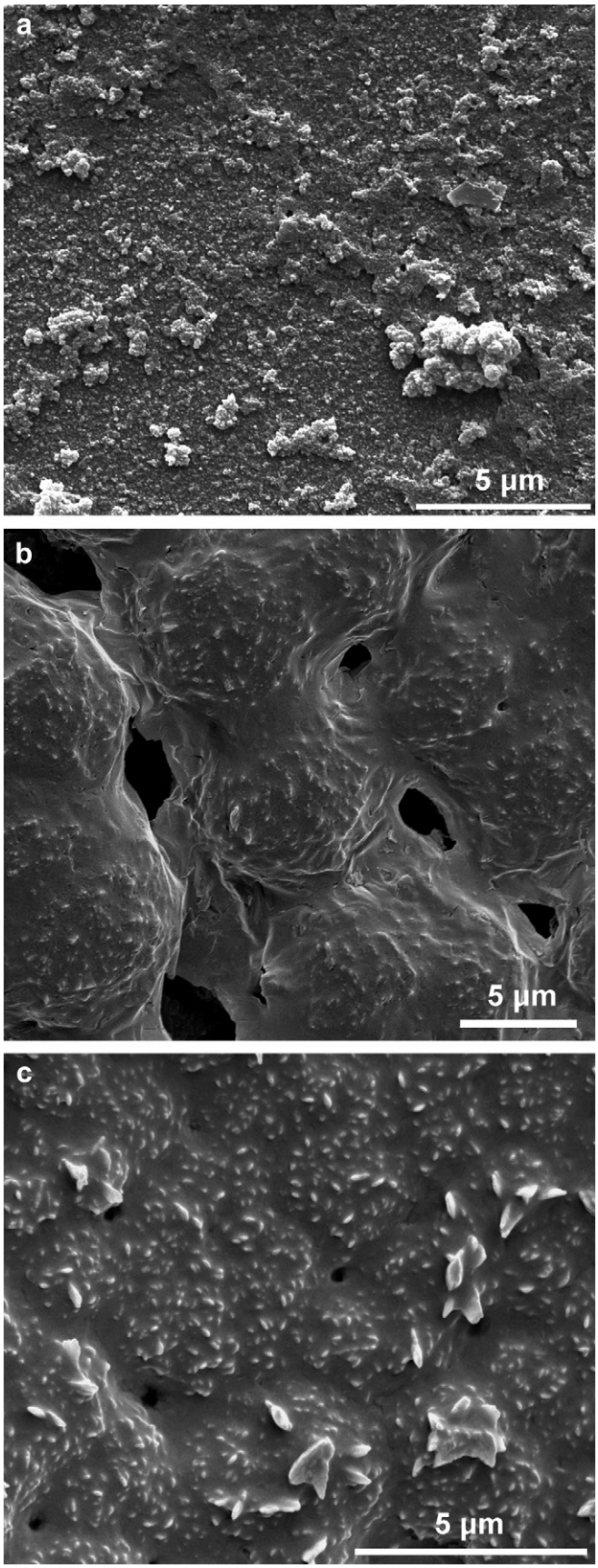

Fig. 7. SEM images of (a) thick Si film after 30 charge–discharge cycles, (b) thin Si film after 120 charge–discharge cycles, and (c) Si–Ag film after 30 charge–discharge cycles.

Si–Ag film. In addition, amorphous silicon structure is recognized be able to buffer the volume expansion and contraction of Si anode [7,12]. The existence of more amorphous phase in Si–Ag film is also responsible for the improvement of cyclability.

Furthermore, we examine the morphologies of the films after galvanostatic discharge–charge tests. As for the sample of thick Si film after 30 cycles testing (Fig. 7(a)), severe pulverization of silicon film happens, resulting in abundant particles dispersed on the Cu/Kapton substrate. This indicates that deep Si nanoparticles in the thick film cannot be effectively cured in the photosintering process and the adhesion of thick silicon layer to the substrate is weak. When silicon layer is reduced to ~1.3 μm, the thin silicon layer comprised of fused Si nanoparticles can attach the substrate tightly. After 120 cycles, although the large pores appear and the surface becomes fluctuant, the peeling of silicon particles is not observed in thin Si film (Fig. 7(b)). Fig. 7(c) shows the surface structure of Si–Ag film after cycling remained relatively uniform and flat compared to thin Si film. It indicates that the volume change in Si–Ag film is suppressed. The addition of Ag nanoparticles does not affect photosintering efficiency, which extends the application range of photosintering approach. Flexible manufacture render photosintering approach promising prospect in LIB application field. Further optimization of silicon films with various thickness and appropriate additive will be done to reach higher reversible capacity and longer cycle life.

4. Conclusion

Silicon films with fused nanoparticles have been successfully prepared by the ANI photosintering approach. The thickness of silicon layer is easily controlled by varying the amount of coating ink under the optimized fabrication conditions. Owing to the close adhesion of the fused silicon nanoparticles to the substrate, thin Si film showed better cyclability relative to thick Si film. The addition of Ag improved the film conductivity and facilitated the formation of amorphous silicon phase, which resulted in the excellent capacity and cycling performance. The present study provides a promising and practicable approach to fabricate the high-performance Si anode materials for the LIB application.

Acknowledgments

This work was funded by the Office of the Secretary of Defense, Contract Number: W911QX-10-C-0044. The authors thank Advanced Materials Engineering Research Institute (AMERI) facility at Florida International University.

Appendix A. Supplementary material

Supplementary material associated with this article can be found, in the online version, at doi:10.1016/j.jpowsour.2012.04.047.

References

[1] J.M. Tarascon, M. Armand, Nature 414 (2001) 359–367.
[2] H. Li, Z. Wang, L. Chen, X. Huang, Adv. Mater. 21 (2009) 4593–4607.
[3] J. Ning, T. Jiang, K. Men, Q. Dai, D. Li, Y. Wei, B. Liu, G. Chen, B. Zou, G. Zou, J. Phys. Chem. C 113 (2009) 14140–14144.
[4] X. Li, A. Dhanabalan, K. Bechtold, C. Wang, Electrochem. Commun. 12 (2010) 1222–1225.
[5] Y. Hamon, T. Brousse, F. Jousse, P. Topart, P. Buvat, D.M. Schleich, J. Power Sources 97–98 (2001) 185–187.
[6] K.T. Lee, Y.S. Jung, S.M. Oh, J. Am. Chem. Soc. 125 (2003) 5652–5653.
[7] J. Cho, J. Mater. Chem. 20 (2010) 4009–4014.
[8] W. Chen, Z. Fan, A. Dhanabalan, C. Chen, C. Wang, J. Electrochem. Soc. 158 (2011) A1055–A1059.
[9] L. Lacroix-Orio, M. Tillard, D. Zitoun, C. Belin, Chem. Mater. 20 (2008) 1212–1214.

[10] X. Yang, Z. Wen, S. Huang, X. Zhu, X. Zhang, Solid State Ionics 177 (2006) 2807–2810.
[11] H. Jung, M. Park, S.H. Han, H. Lim, S.K. Joo, Solid State Commun. 125 (2003) 387–390.
[12] T. Takamura, S. Ohara, M. Uehara, J. Suzuki, K. Sekine, J. Power Sources 129 (2004) 96–100.
[13] M.S. Park, G.X. Wang, H.K. Liu, S.X. Dou, Electrochim. Acta 51 (2006) 5246–5249.
[14] K.L. Lee, J.Y. Jung, S.W. Lee, H.S. Moon, J.W. Park, J. Power Sources 129 (2004) 270–274.
[15] J.P. Maranchi, A.F. Hepp, P.N. Kumta, Electrochem. Solid-state Lett. 6 (2003) A198–A201.
[16] M. Ledinsky, A. Vetushka, J. Stuchlik, T. Mates, A. Fejfar, J. Kocka, J. Stepanek, J. Non-Cryst. Solids 354 (2008) 2253–2257.
[17] Y. Kimura, T. Katoda, Appl. Surf. Sci. 117–118 (1997) 790–793.
[18] H. Li, X. Huang, L. Chen, G. Zhou, Z. Zhang, D. Yu, Y.J. Mo, N. Pei, Solid State Ionics 135 (2000) 181–191.
[19] K.F. Dombrowski, I.D. Wolf, B. Dietrich, Appl. Phys. Lett. 75 (1999) 2450–2451.
[20] M. Holtz, W.M. Duncan, S. Zollner, R. Liu, J. Appl. Phys. 88 (2000) 2523–2528.
[21] R. Liu, M. Canonico, Microelectron. Eng. 75 (2004) 243–251.
[22] P. Limthongkul, Y. Jang, N.J. Dudney, Y. Chiang, Acta Mater. 51 (2003) 1103–1113.
[23] Z. Song, H. Zhan, Y. Zhou, Angew. Chem. Int. Ed. 49 (2010) 8444–8448.
[24] Q. Sun, B. Zhang, Z.W. Fu, Appl. Surf. Sci. 254 (2008) 3774–3779.
[25] H. Yoo, J.I. Lee, H. Kim, J.P. Lee, J. Cho, S. Park, Nano Lett. 11 (2011) 4324–4328.
[26] M.T. McDowell, S.W. Lee, I. Ryu, H. Wu, W.D. Nix, J.W. Choi, Y. Cui, Nano Lett. 11 (2011) 4018–4025.